



An experimental study of the effect of off-fault damage on the velocity of a slip pulse

Ronald L. Biegel,¹ Charles G. Sammis,¹ and Ares J. Rosakis²

Received 15 June 2007; revised 16 October 2007; accepted 4 December 2007; published 8 April 2008.

[1] The effect of off-fault damage on the speed of ruptures propagating on faults in photoelastic Homalite plates was measured using high-speed digital photography. The off-fault damage was composed of a network of fractures introduced by thermally shocking the Homalite in liquid nitrogen. The mode II rupture speed measured in damaged Homalite was significantly lower than the limiting Rayleigh speed of $v_r = 0.92 v_s$, even after the shear wave speed v_s was reduced to a value appropriate for the fracture-damaged Homalite. The additional slowing is most likely caused by frictional sliding on preexisting cracks, especially since we did not observe the generation of new fractures. The spatial extent of the interaction between the rupture and the off-fault damage was measured using samples in which the damage was limited to a band of width $2w$ centered on the fault and also using damaged samples containing a band of undamaged Homalite centered on the fault. By measuring the rupture velocity as a function of w , the interaction between the rupture and off-fault damage was observed to be limited to a distance of about 1 cm from the fault plane. This agrees with the spatial extent of Coulomb failure near the tip of a dynamic slip pulse predicted by the analytic model developed by Rice et al. (2005).

Citation: Biegel, R. L., C. G. Sammis, and A. J. Rosakis (2008), An experimental study of the effect of off-fault damage on the velocity of a slip pulse, *J. Geophys. Res.*, 113, B04302, doi:10.1029/2007JB005234.

1. Introduction

[2] A key challenge in earthquake physics is to understand how fault zone structure affects rupture mechanics. Most earthquake models represent a fault as two planar surfaces in frictional contact and rupture as a shear crack propagating along the interface. Fracture energy in these models is dissipated on the fault plane as friction decreases from its static value to a lower dynamic value [Palmer and Rice, 1973; Rice et al., 2005]. Real faults, many exhumed from seismogenic depths, have more complex structures with localized slip zones tens of centimeters wide bordered by highly fractured damage zones that often extend from tens to hundreds of meters from the main fault plane [Sammis et al., 1987; Chester et al., 1993; Brune, 2001; Ben-Zion and Sammis, 2003; Biegel and Sammis, 2004; Chester et al., 2004, 2005; Rice, 2006].

1.1. Plasticity Model for the Effect of Off-Fault Damage on the Rupture Speed of a Growing Crack

[3] Recent earthquake models by Andrews [2005], Templeton and Rice [2006], and Viesca et al. [2006] approximate the mechanical behavior of this off-fault

damage with ideal plasticity in which the fault zone rocks yield when stresses reach Coulomb failure. They find that this off-fault plastic flow dissipates sufficient energy to significantly reduce the velocity of the main rupture. However, these models differ from real earthquakes in two ways. First, ideal plasticity assumes that stresses never exceed the Coulomb slip criterion. This is not the case in micromechanical damage mechanics, which predicts that, while slip on cracks in the fault zone begins at the Coulomb level, stresses can rise above the Coulomb level between damage initiation and failure [Ashby and Sammis, 1990]. Representing the strain associated with slip on the myriad of small cracks in the damage zone with ideal plasticity gives a maximum off-fault strain, and such models may overestimate the effect of off-fault damage on rupture velocity. A second limitation of the Andrews [2005] and Templeton and Rice [2006] plasticity models is that they assume a growing crack-like rupture while recent studies of the slip function for earthquakes find dislocation-like “slip pulses” [Heaton, 1990]. While both the strength of a crack tip singularity and the extent of off fault plasticity grow monotonically in crack-like models, Rice et al. [2005] have shown that both reach a stable value for a slip pulse.

1.2. An Analytic Model for the Stress Field in the Vicinity of a Propagating Slip Pulse

[4] Rice et al. [2005] formulated an analytic model for a two-dimensional slip pulse having finite length L , and slip-weakening distance R that propagates at a fixed velocity along a fault in an elastic medium (Figure 1a). As illustrated in Figure 1b, this model predicts the off-fault stresses as a

¹Department of Earth Sciences, University of Southern California, Los Angeles, California, USA.

²Graduate Aeronautical Laboratories, California Institute of Technology, Pasadena, California, USA.

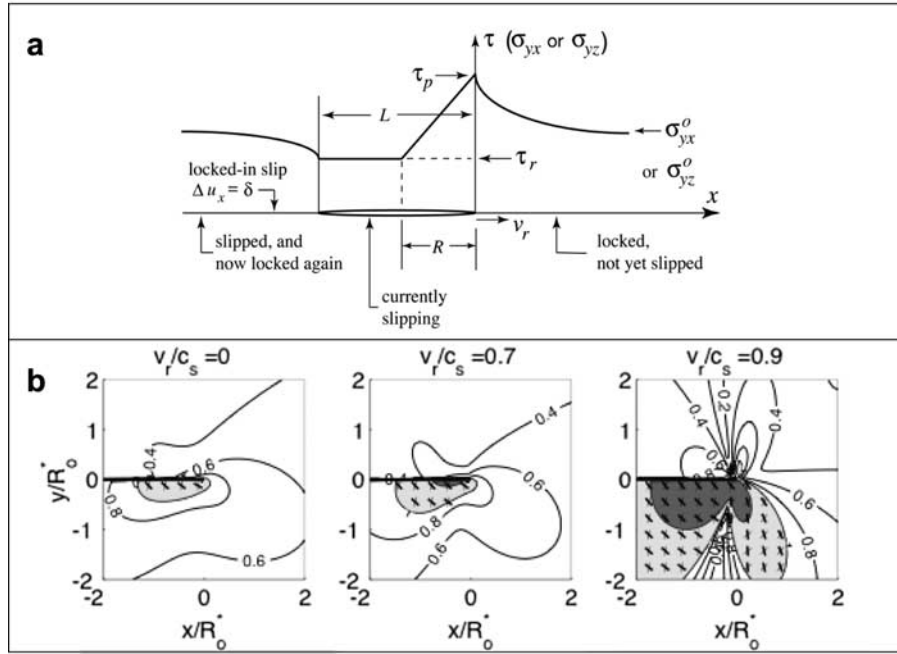


Figure 1. (a) Shear stress near the tip of a propagating slip pulse. The parameters τ_p and τ_r are peak and residual shear stresses, and σ_{yx}^0 or σ_{yz}^0 is the initial shear stress. R is the slip weakening distance. L is the length of the pulse [from Rice *et al.*, 2005]. (b) Contour plot of the maximum Coulomb stress as a function of position around the tip of a slip pulse. Each panel is for a different rupture velocity as indicated. Within shaded areas the maximum Coulomb stress exceeds one, meaning slip on the most favorably oriented preexisting fracture is possible [from Rice *et al.*, 2005].

function of rupture velocity and the initial stress state. Analytic expressions for the stress field near the tip of a propagating mode II (or mode III) slip pulse are given in dimensionless form, where lengths are scaled by R_O^* , the value of R in the limit of low rupture speed and low stress drop, and in the limit of an infinitely long slip pulse. This scaling length is given by

$$R_O^* = \frac{9\pi}{16(1-\nu)} \frac{\mu G}{(\tau_p - \tau_r)^2} \quad (1)$$

where ν is the Poisson ratio, μ is the shear modulus, τ_p and τ_r are peak and residual stresses, and the fracture energy G is

$$G = \delta_1 (\tau_p - \tau_r) \quad (2)$$

Equation (2) assumes an exponential decrease in friction with displacement [Palmer and Rice, 1973]. Substituting equation (2) for G in equation (1) and assuming $\tau_r \ll \tau_p$ gives

$$R_O^* \approx \frac{9\pi}{16(1-\nu)} \frac{\mu \delta_1}{f \sigma_n} \quad (3)$$

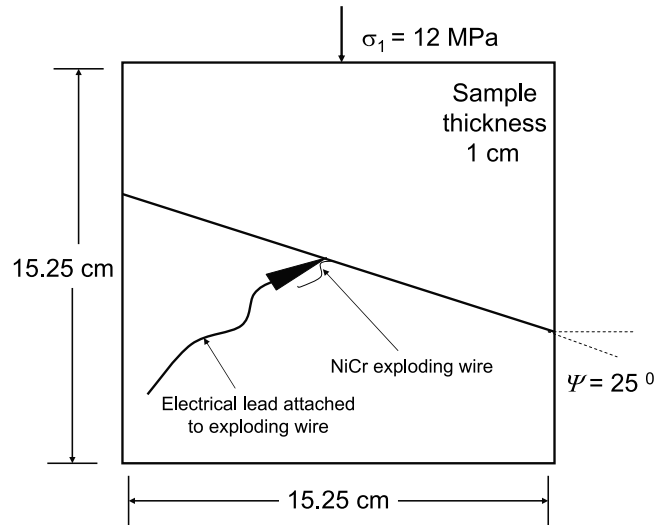


Figure 2. Geometry of Homalite samples. The fault angle was $\Psi = 25^\circ$ to the horizontal, and a compressive uniaxial load of $\sigma_1 = 12$ MPa was applied to top and bottom of the sample. Rupture was nucleated by exploding a NiCr wire in a 0.1 mm hole drilled through the sample at the center of the fault.

Table 1. Material Properties of Homalite 100^a

Material Properties of Homalite 100	Static	Dynamic
Young's modulus E , ^b GPa	3.9	5.2
Shear modulus μ , ^b GPa	1.4	1.9
Poisson's ratio ν , ^b	0.35	0.34
Density ρ , ^b kg/m ³	1230	
Friction f , ^c	0.6	0.2
P wave velocity, v_p , ^c m/s		2498
S wave velocity, v_s , ^c m/s		1200
Characteristic displacement d_c , ^c m		10^{-5}

^aStatic values for elastic moduli were calculated using standard relations for an isotropic linear elastic solid. Dynamic values for elastic moduli were measured with ultrasonic transducers.

^bSamudrala and Rosakis [2003].

^cXia et al. [2004].

where f_s is the coefficient of static friction, δ_1 is the characteristic displacement, and σ_n is the normal stress.

[5] Rice et al. [2005] fit their model to data from Heaton [1990] and estimated R^* for several large earthquakes to be in the range 1.3 to 36 m. Note in Figure 1b that the stress field is sensitive to the rupture velocity v_r . In most of our experiments v_r was greater than $0.70 v_s$ but less than the Rayleigh limit $0.92 v_s$ so that Figures 1b (middle) and 1b (right) best represent the stress state near the fault in our experiments. Hence we expect that Coulomb slip should extend to distances on the order of R^* . The primary objective of the experiments presented here is to measure the spatial extent of the interaction between the stress field at the tip of the propagating slip pulse and the damage for comparison with this model-based prediction.

1.3. Propagation of a Slip Pulse on a Fault in Damaged Homalite

[6] In these experiments, we use high-speed digital photography to explore the effect of off-fault fracture damage on the velocity of spontaneous fault rupture in photoelastic Homalite plates. These laboratory experiments more realistically represent earthquakes than do current numerical models because (1) our laboratory fault zone is composed of an array of fractures and (2) our ruptures propagate as slip pulses, which is significant for two reasons. First, Heaton [1990] proposed that a slip pulse model could explain why seismic risetimes were only a fraction of an earthquake's rupture duration while crack-like models could not. Second, Zheng and Rice [1998] found that for conditions expected at seismogenic depths in the Earth, ambient stresses are too weak to support crack-like ruptures and that earthquakes should propagate as slip pulses.

[7] Lu et al. [2006, 2007] observed laboratory ruptures in experiments with Homalite samples using an experimental configuration similar to the one used here. They concluded that the model of Zheng and Rice [1998] correctly predicted the modes of rupture that they observed in their experiments. As the normal load and the inclination angle of the fault surface decreased, the rupture transitioned from a growing crack to a slip pulse. For conditions closest to our experiments (a fault inclination angle of 25° and a normal load of 10 MPa) they observed that ruptures propagated as slip pulses as predicted by the model of Zheng and Rice [1998]. For experimental conditions that

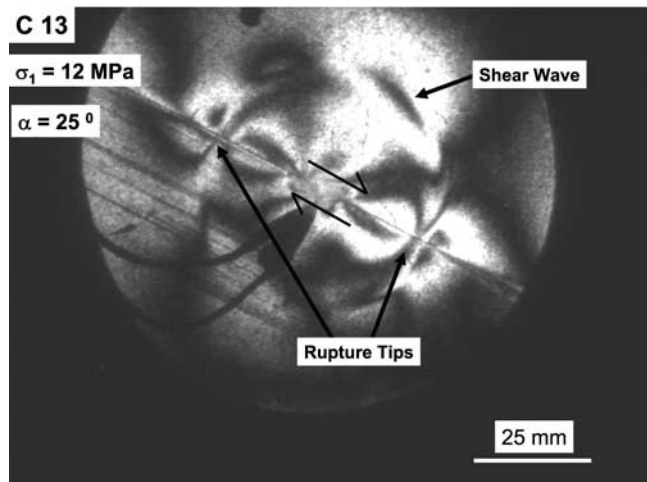


Figure 3. A digital image from experiment C-13. Tips of the bilateral rupture appear as dark points surrounded by fringes that propagate to the left and right along the fault from the central nucleation point. The shear wave fringe can be most clearly seen propagating toward the top left corner of the field of view.

exactly matched ours, (inclination angle of 25° and a normal load of 12 MPa) Lu et al. [2006] performed the Zheng and Rice [1998] analysis and found that a rupture propagated either as a slip pulse or a dying slip pulse. This

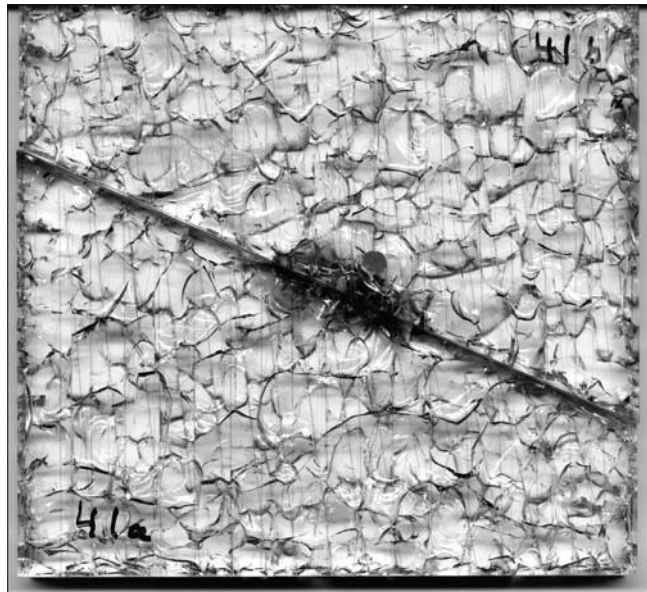


Figure 4. A digital scan of the all-damaged sample used in experiment H-50. The image shows the top and bottom pieces of the sample with their dense fracture network. The faint vertical and horizontal parallel lines on the surface were made by scoring with a knife before immersion in liquid nitrogen. The dark traces in the center along the fault are from the nucleation explosion.

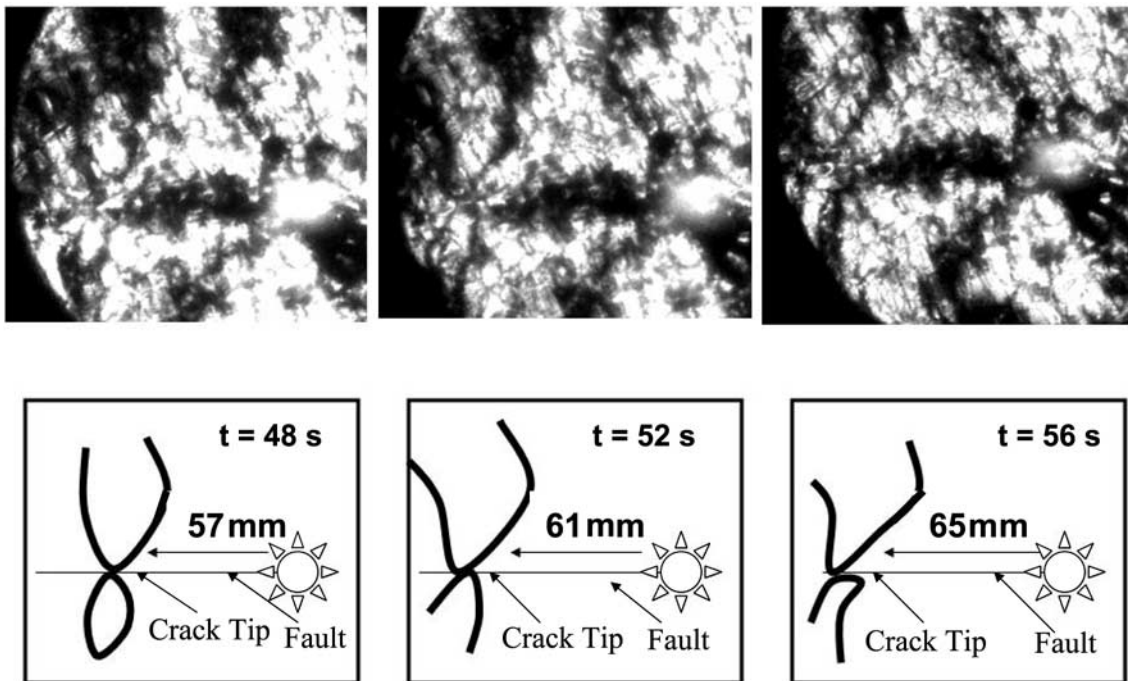


Figure 5. (top) Three successive digital images from experiment H-50 rotated 25° orienting the right-lateral fault parallel to page bottom. The dark spot on the fault plane is the left propagating rupture tip having fringes of equal shear stress extending above and below the rupture. (bottom) Rupture tip and fringes drawn to help identify them in the digital image. Elapsed time t and distance from nucleation point are also given. The sunburst to the right of center on the fault shows where the nucleation explosion appears in the digital image.

implies that our experiments realistically simulate actual earthquakes.

[8] Physical properties of the photoelastic Homalite 100 used in these experiments are given in Table 1. Substitution of these values into equation (3) gives $R_{\delta}^* \approx 0.9$ cm, so we expect the interaction between the crack tip stress field and the off-fault damage in our experiments to extend to distances on the order of 1 cm.

2. Experimental Procedure

[9] The samples for our experiments were made from square photoelastic Homalite 100 plates (15.25 cm \times 15.25 cm \times 1 cm) cut at an angle of 25° to form a fault as in the work by Xia *et al.* [2004] and Biegel *et al.* [2007] (Figure 2). Each sample had a 0.1 mm diameter hole at the center of the fault into which a nickel chromium wire was inserted before the samples were placed into a loading frame.

[10] We introduced a network of fractures (damage) into the Homalite samples by thermal shock in liquid nitrogen. To control the density of the crack network, we used a razor knife to score a grid of surface scratches on the part of the sample to be damaged. The portion of the sample to be damaged was then immersed in liquid nitrogen for about 30 s. Samples were prepared with four different damage configurations: undamaged samples (Figure 3), all-damaged samples (Figures 4, 5, and 6), samples with a band of

damage surrounding the fault (Figures 7a and 7b), and all-damaged samples except for an undamaged band surrounding the fault (Figures 8a and 8b).

[11] Fracture damage was quantified using standard stereology techniques described by Underwood [1970]. Test lines were drawn across the damaged region and the number of crack intersections per unit line length P_L was determined. Since the cracks bound “cells” of average diameter $\bar{L}_3 = 1/P_L$, the average crack diameter is about $\langle a \rangle = \bar{L}_3/2$ and the area of an average crack is $\bar{A}_{cr} = \pi \langle a^2 \rangle$. The surface area of cracks per unit volume is $S_V = 2P_L$ and hence the number of cracks per unit volume is $N_V = S_V / \bar{A}_{cr}$. Crack damage in O’Connell and Budiansky’s [1974] analysis of elastic moduli is defined as $\varepsilon = N_V \langle a^3 \rangle$, which is simply related to the Ashby and Sammis [1990] definition of initial damage D_0 as $D_0 = (4\pi/3)\varepsilon$. Fracture damage parameters measured for the all-damaged and partially damaged samples are summarized in Table 2. For the all-damaged sample, the measured value of $\varepsilon = 0.3$ which, according to the O’Connell and Budiansky [1974] model, corresponds to a ratio of fractured S wave velocity \bar{v}_s to unfractured velocity v_s of $\bar{v}_s/v_s = 0.7$. This value is close to the reduction in S wave velocity measured in the experiments described below.

[12] The experimental apparatus shown in Figure 9 is a plane polariscope in which contours of equal shear stress appear as dark fringes on the sample. The laser emits a continuous collimated beam with a wavelength of 514 nm

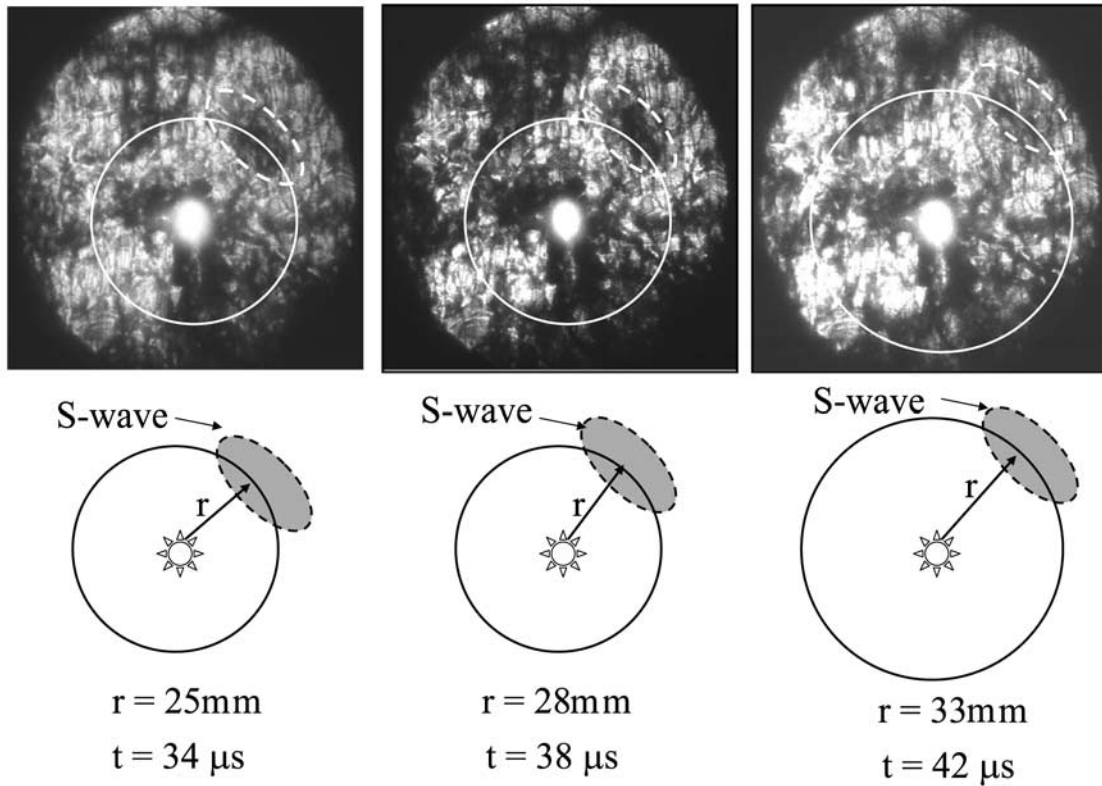


Figure 6. (top) Three successive digital images from experiment H-70 rotated 25° orienting the right-lateral fault parallel to page bottom. In each image the shear wave can be seen as a dark ellipse propagating toward the upper right of the field of view. Another lobe can be seen propagating to the upper left. (bottom) Right propagating shear wave indicated as a grey ellipse to help identify it in the digital image. Elapsed time t and distance r from the nucleation point are also shown.

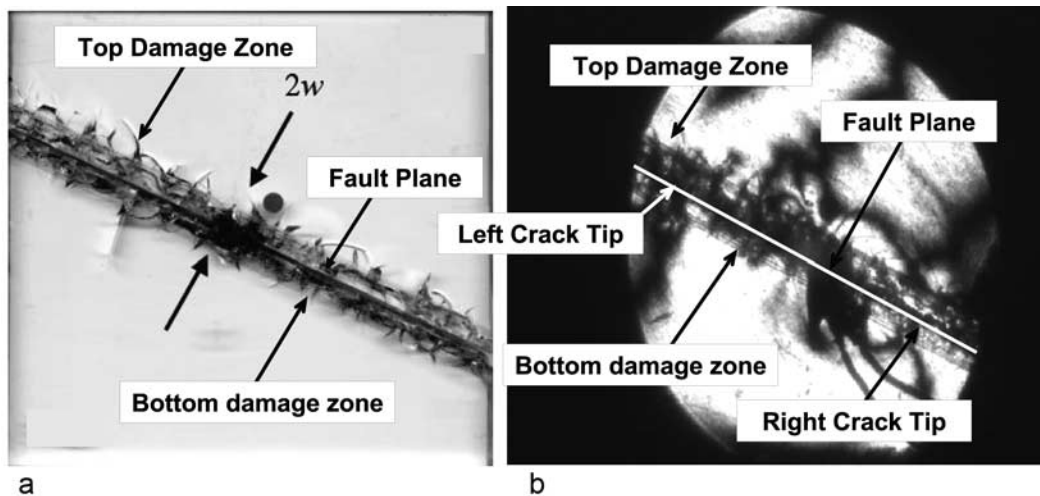


Figure 7. (a) A digital scan of a sample with damage bands of half width $w_d = 0.5$ cm made by dipping the edges in liquid nitrogen. The dark traces in the center along the fault are from the nucleation explosion. (b) A digital image from an experiment with damage bands. A rupture tip from the bilateral rupture appears as a dark spot on the fault surrounded by fringes and propagating to the left and right from a central nucleation point. The shear wave in this experiment has propagated out of the field of view. Sense of motion along fault is right lateral.

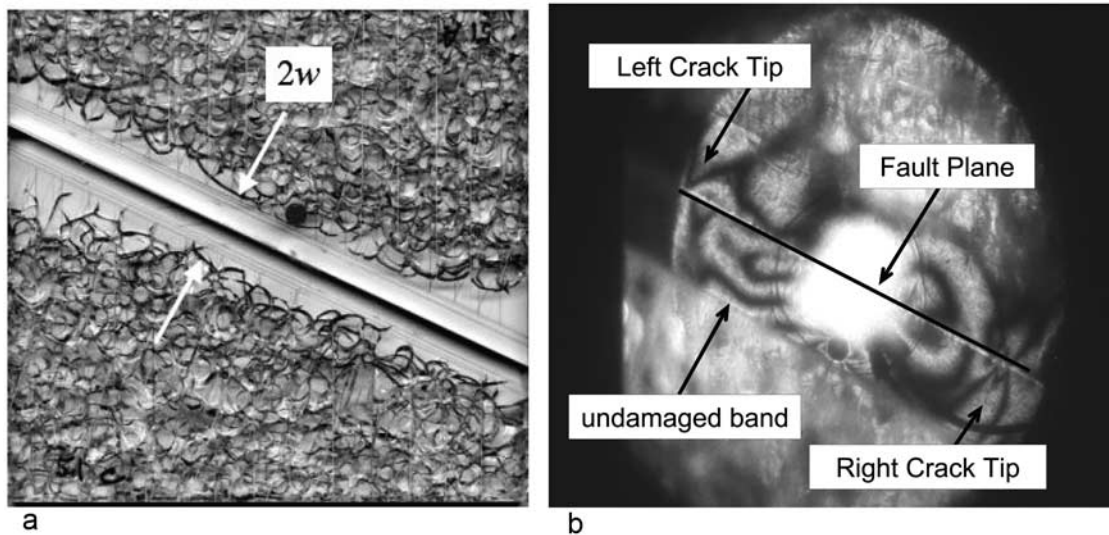


Figure 8. (a) A digital scan of the sample with undamaged bands of half width $w_d = 0.5$ cm made by dipping all of the sample in liquid nitrogen except the edges. (b) A digital image from experiment H-52 with sample having undamaged bands of half width $w_u = 2$ cm. The bilateral rupture tips clearly appear as dark spots on the fault surrounded by fringes propagating to the left and right from a central nucleation point. The shear wave in this experiment has propagated out of the field of view. Sense of motion along fault is right lateral.

that passes through a polarizer and the sample. It then passes through another polarizer to a beam splitting mirror serving two identical digital cameras. Each camera records 8 digital images at a nominal rate of one frame every $2 \mu\text{s}$ [Dally and Riley, 2005].

[13] At the start of each experiment the sample was loaded to a uniaxial stress of 12 MPa. A capacitor bank was then discharged to vaporize the wire and nucleate a rupture by reducing the normal stress along about 1.5 cm of the fault plane. The capacitor discharge was also used to trigger the cameras. After each experiment the decrease in uniaxial load was recorded.

[14] The rupture tips could be identified in the digital photographs as areas of intense fringe concentration (high shear stress) that moved along the fault plane in successive frames. Fringes associated with the shear wave could usually be identified as segments of a circle centered on the explosion. These segments corresponded to the maxi-

mum lobes of the double-couple S wave radiation pattern generated by slip acceleration at the nucleation site.

[15] We first tested samples without damage for comparison with Xia *et al.* [2004] and Biegel *et al.* [2007]. A second series of experiments used all-damaged samples to observe the effect of damage on the rupture and shear wave velocities. The rest of the experiments used samples having damaged or undamaged bands of different widths to determine the spatial extent of the interaction between the stress field at the rupture tip and the off-fault damage.

3. Experimental Results

[16] For each experiment, we observed bilateral ruptures and the positions of the crack tips and shear wave fringes were identified in each frame of the sequence of digital photos. The propagation distances were plotted as a function of time to find the rupture speed, v_r , and the shear wave

Table 2. Crack Density Data^a

Sample	P_L , mm	L_3 , mm	$\langle a \rangle$, mm	A_{CR} , mm	S_v , $\text{mm}^2 \text{mm}^{-3}$	N_v	ϵ
S-41	0.13	7.9	3.9	47.8	0.25	0.005	0.31
	0.17	5.9	2.9	26.4	0.33	0.012	0.32
	0.13	8.9	4.4	61.6	0.23	0.004	0.31
	0.16	6.2	3.1	30.7	0.32	0.01	0.32
S-61a	0.14	6.9	3.4	37.0	0.29	0.008	0.31
S-61b	0.14	7.3	3.7	42.1	0.27	0.006	0.32

^aFour traverses were taken across one sample half of the S-41 all-damage sample. One traverse each was made across sample S-61 top and bottom sample halves. A point was counted when a crack surface intersected a grid line. P_L is points per unit line, L_3 is mean intersect length, $\langle a \rangle$ is average crack radius, A_{CR} is average crack surface, S_v is total crack surface per unit volume, N_v is number of cracks per unit volume, and $\epsilon = N\langle a^3 \rangle$ is the crack density parameter [O'Connell and Budiansky, 1974].

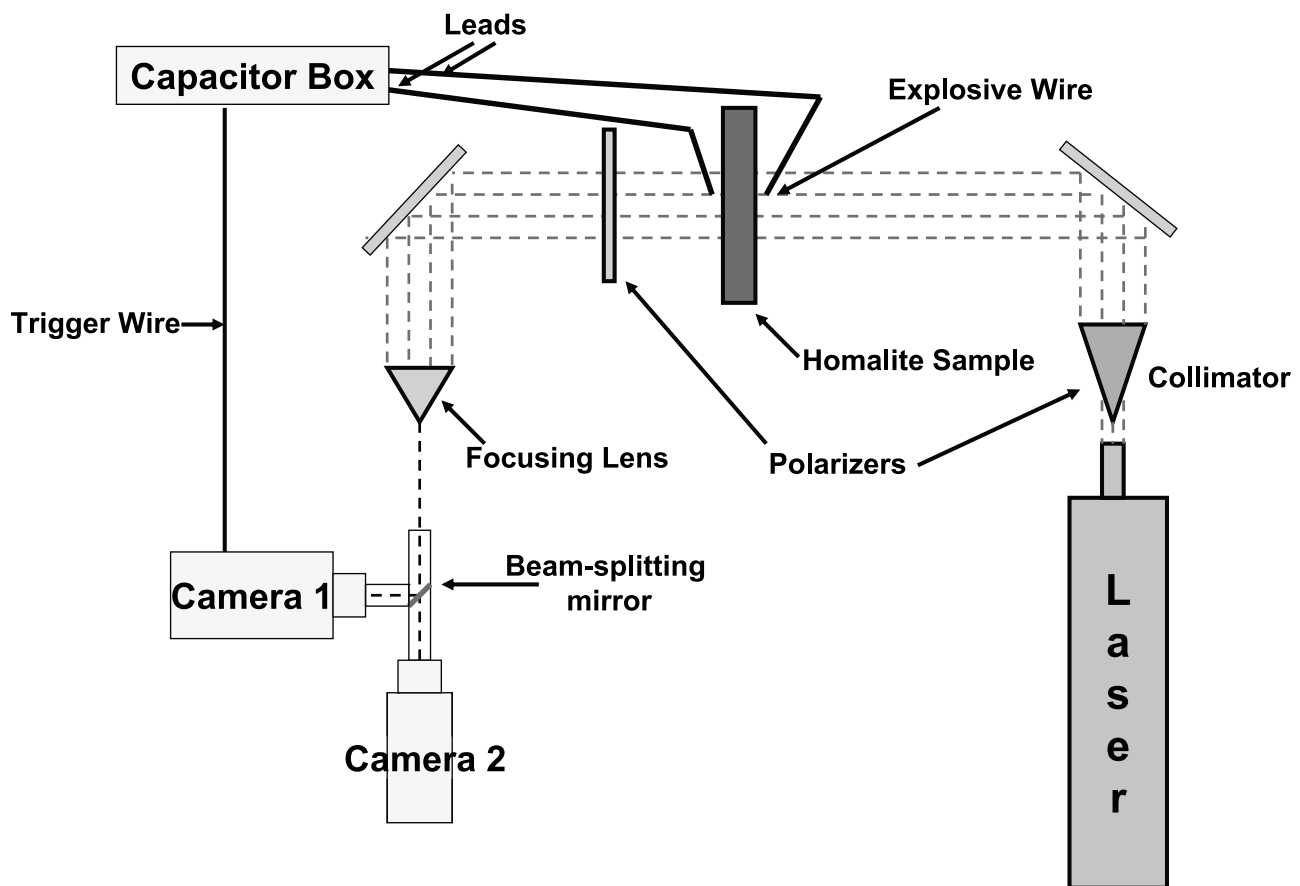


Figure 9. Diagram of experimental setup.

velocity, v_s . The velocities measured in all experiments are given in Tables 3, 4, and 5. A few rupture velocities could not be measured as indicated in Tables 3–5.

3.1. Undamaged Samples

[17] Two experiments (C-13 and H-43) used undamaged samples (Figure 3). For experiment H-43, the positions of the two rupture tips and the S wave are plotted as functions of time in Figures 10a and 10b. The S wave velocity was

1220 m s^{-1} , consistent with known values for Homalite [Samudrala and Rosakis, 2003; Xia *et al.*, 2004]. The rupture speed was 1110 m s^{-1} ($0.91v_s$), consistent with previous measurements by Xia *et al.* [2004] and Biegel *et al.*

Table 3. Experiments Classified by the Spatial Extent of Damage in the Sample^a

Experiments	V_r , m/s	V_s , m/s	V_r/V_s
<i>No Damage</i>			
C-13	left 1150	1280	0.90
C-13	right 1150	1280	0.90
H-43	left 1110	1220	0.91
H-43	right 1090	1220	0.90
<i>All-Damaged</i>			
H-50	left 900	1030	0.87
H-50	right V_r could not be measured	—	—
H-53	left 830	—	—
H-53	right V_r could not be measured	—	—
H-70	left 720	970	0.74
H-70	right V_r could not be measured	—	—
HH-7	left 820	1000	0.84
HH-7	right 860	1000	0.84

^aExperiment name, direction of rupture propagation (left or right), rupture speed v_r , shear wave velocity v_s , and ratio of v_r/v_s . All experiments were run at 12 MPa, the remote uniaxial stress, not the normal stress resolved onto the main fault.

Table 4. Experiments Classified by the Half Width of the Damage Band w_d in the Sample^a

Experiments	Rupture Direction	V_r , m/s
<i>Damage Half Width = 1/2 cm</i>		
H-54	left	930
H-54	right V_r could not be measured	—
H-55	left	1000
H-55	right	930
H-58	left	880
H-58	right	830
<i>Damage Half Width = 1 cm</i>		
H-59	left	680
H-59	right	660
H-62	left	830
H-62	right	710
<i>Damage Half Width = 2 cm</i>		
H-61	left	910
H-61	right	900
H-67	left	880
H-67	right V_r could not be measured	—
HH-10	right	850

^aExperiment name, direction of rupture propagation and rupture speed v_r . All experiments were run at a uniaxial stress of 12 MPa.

Table 5. Experiments Classified by the Half Width of Undamaged Band w_u in the Sample^a

Experiments	Rupture Direction	V_r (m/s)
<i>Undamaged Half Width = 0.5 cm</i>		
H-51	left	1000
H-51	right	1030
<i>Undamaged Half Width = 2 cm</i>		
H-52	left	1010
H-52	right	1050

^aExperiment name, direction of rupture propagation (left or right), and rupture speed v_r . All experiments were run at a uniaxial stress of 12 MPa.

[2007]. Rupture and shear wave velocities for the experiments using undamaged samples are given in Table 3.

3.2. All-Damaged Samples

[18] The experiments using “all-damaged” samples were designed to see if off-fault damage could slow the rupture speed significantly below the Rayleigh limit ($v_R = 0.92v_s$) where v_s is the shear wave velocity in the damaged Homalite. Four experiments (H-50, H-53, H-70, and HH-7), used all damaged samples prepared by completely immersing the prescored Homalite plates into liquid nitrogen (Figures 4, 5, and 6).

[19] For sample HH-7, the positions of the crack tips and S wave are plotted as functions of time in Figure 11. As is evident in Figures 5 and 6, stress concentrations due to the damage make it difficult to pick out the rupture front and S wave. We were able to make these picks by producing a movie of carefully aligned successive computer images and identifying moving perturbations in the pattern. While it is difficult to show this in single frames, we have identified the rupture front in three successive images in Figure 5 and the S wave in another three successive frames in Figure 6.

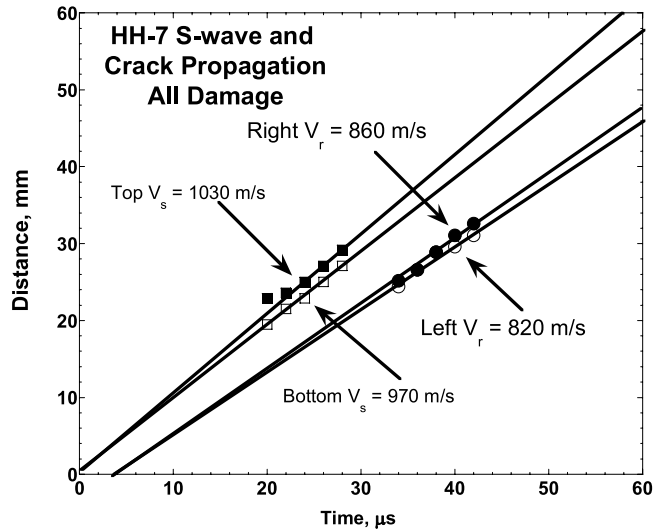


Figure 11. Positions of the rupture tips and the S wave as functions of time for all-damaged sample experiment HH-7. (a) Left propagating rupture tip. (b) Right propagating rupture tip.

[20] The average rupture velocity in Figure 11 was $\sim 840 \text{ m s}^{-1}$, or $\sim 73\%$ of the undamaged value, and the average S wave velocity was 1000 m s^{-1} or 80% of the undamaged value. The ratio $v_r/v_s = 0.84$ is significantly below the Rayleigh limit of 0.92. Note that we have used the reduced value of v_s corresponding to the damaged Homalite. The implication is that v_r has been reduced beyond the effect of the lower v_s , presumably reflecting energy loss in the off-fault damage.

3.3. Samples With Damage Bands

[21] In order to determine the distance to which Coulomb slip extends from the fault plane, samples were prepared with damage bands surrounding the fault plane having

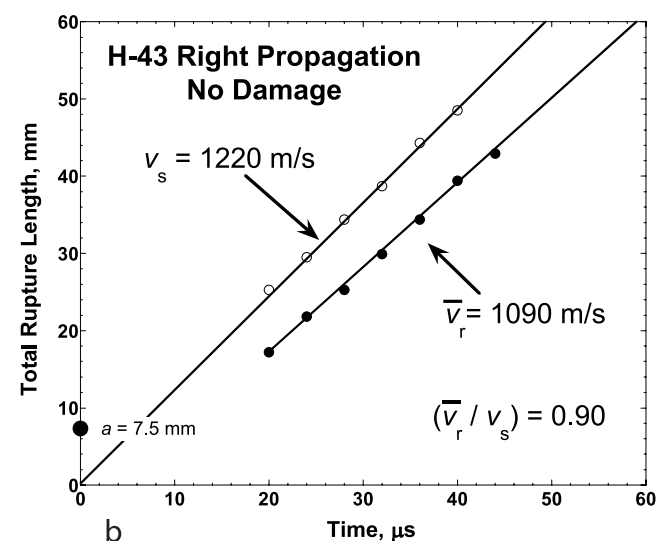
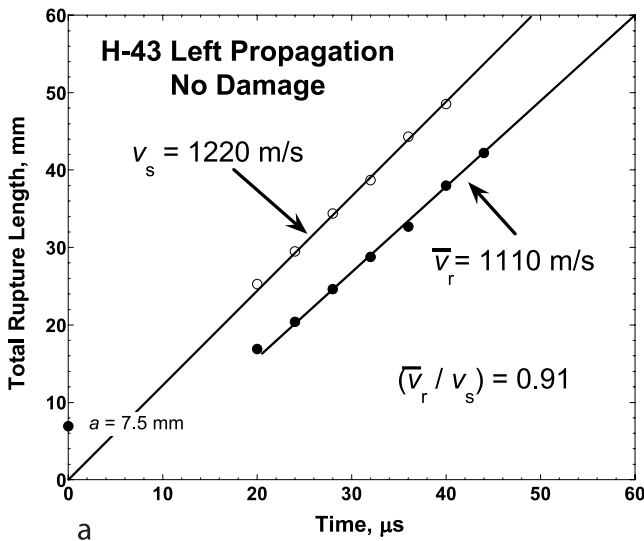


Figure 10. Positions of the rupture tips and the S wave as functions of time for experiment H-43. (a) Left propagating rupture tip. (b) Right propagating rupture tip. Point $a = 0.7 \text{ mm}$ indicates the half length of the nucleating crack inferred from postexperiment inspection of the samples.

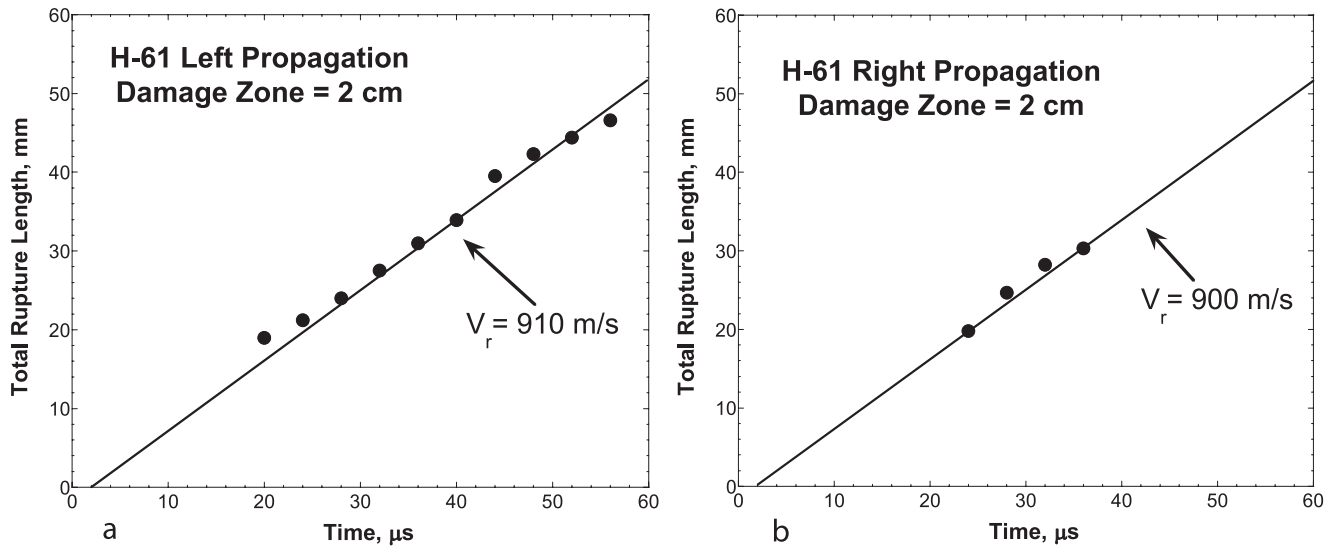


Figure 12. Position of the rupture tip as a function of time for experiment H-61 that had a 2 cm wide damage band. (a) Left propagating rupture tip. (b) Right propagating rupture tip.

widths of 0.5, 1.0 and 2.0 cm. Our hypothesis is that as the damage bands become wider, more energy is dissipated off-fault and the rupture velocity should become slower. This progressive slowing should stop when the width of the damage zone is equal to the maximum distance at which Coulomb slip occurs on the off-fault cracks. When the width of the damage band exceeds the spatial extent of off-fault Coulomb slip on the cracks, then any additional increases in damage width should have no effect on the rupture velocity.

[22] Figure 12 shows the positions of the rupture tips and S wave as functions of time for sample H-61. Rupture

velocities for all samples with damage bands are given in Table 4.

3.4. Samples With Undamaged Bands

[23] We also tested samples having undamaged bands surrounding the fault with widths of 0.5 and 2.0 cm. (Figures 8a and 8b). In these cases, all of the sample except the edge along the fault plane were scored and dipped in liquid nitrogen. The hypothesis in this case is that the off-fault damage will not affect the rupture velocity until it is close enough to the fault plane to allow Coulomb slip on the fractures. Figure 13 shows the positions of the crack tips

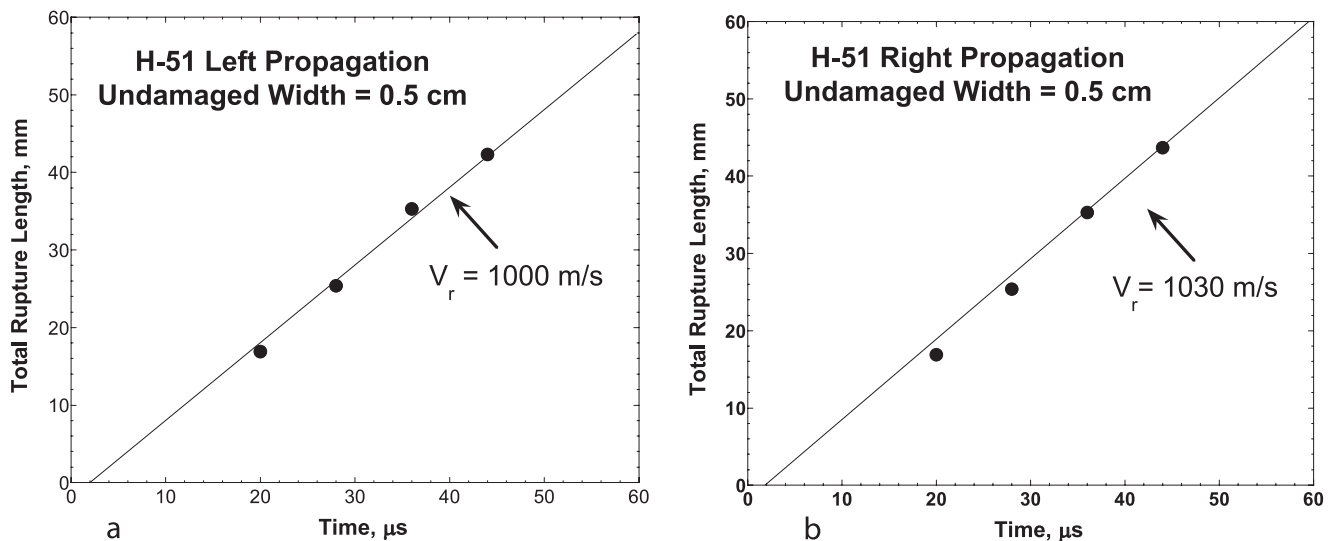


Figure 13. Position of the rupture tip as a function of time for experiment H-51 that had an 0.5 cm wide undamaged band surrounding the fault plane. (a) Left propagating rupture tip. (b) Right propagating rupture tip.

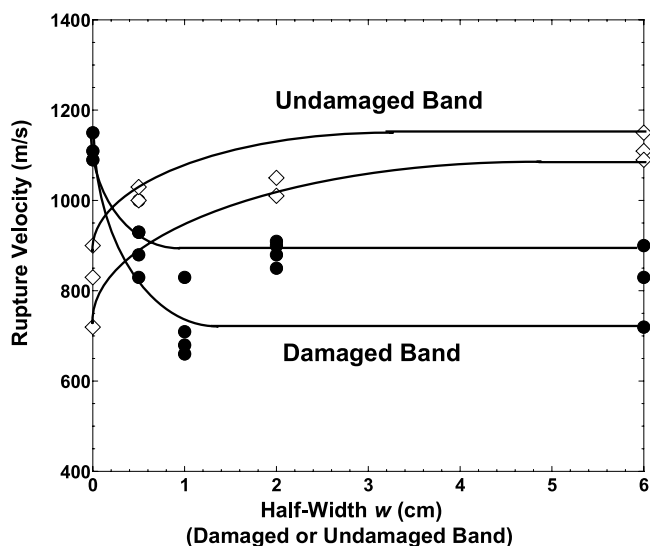


Figure 14. A plot of the rupture speed v_r as a function of the half width w of the damaged (or undamaged) band. Undamaged samples are considered to have an undamaged band half width comparable to the size of the sample, or a damage band of zero half width. All-damaged samples are considered to have a damage band comparable to the width of the sample, or an undamaged band of zero width. Therefore velocities in the undamaged or all-damaged samples appear on both the right and left sides of the graph. Samples with damage bands show a decrease in v_r with an increase in damaged half width w_d . Samples with undamaged bands show an increase in v_r with an increase in undamaged half width w_u . Note that v_r decreases for damaged bands less than ~ 1 cm, reaching a stable rupture speed for larger values. Similarly, v_r increases for undamaged bands less than ~ 1 cm and reaches a stable rupture speed for larger values.

and S wave as functions of time curve for experiment H-51 Rupture velocities for all our experiments using undamaged bands are given in Table 5.

3.5. An Experimental Estimate of R_0^*

[24] The results of the experiments with samples having damaged and undamaged bands from Tables 3–5 are summarized in Figure 14, which shows the rupture speed v_r as a function of the half width w of the band. Experiments using samples with no damage (C-13 and H-43) can be viewed either as having an undamaged band with a half width comparable to the size of the sample and plotted on the right-hand side of Figure 14 or as having a damage band of zero half width and plotted on the left-hand side of Figure 14. Similarly, the experiments having all-damaged samples (H-50, H-53, and H-70) can be viewed as having a damage band comparable to the width of the sample, or an undamaged band of zero width, and are plotted accordingly on Figure 14.

[25] Results from the samples with damage bands show a decrease in v_r with an increase in damaged half width w_d . Experiments with samples having with undamaged bands show an increase in v_r with an increase in undamaged half

width w_u . Note that v_r decreases for w_d less than about 1 cm, reaching a stable rupture speed for larger values. Similarly, v_r increases for w_u less than about 1 cm, and reaches a stable rupture speed for larger values. The implication is that the region of Coulomb slip extends to a distance about 1 cm from the fault plane, in agreement with our above prediction for R_0^* using the Rice *et al.* [2005] model.

4. Discussion

[26] Our experiments show that off-fault damage can reduce rupture speed substantially below the Rayleigh limit of $0.92 v_s$, even when v_s has been reduced to its damaged value. The implication is that mechanisms beyond the simple reduction of the shear modulus contribute to the observed reduction in rupture speed. The most likely explanation is that friction due to Coulomb slip on fracture surfaces dissipates a portion of the energy flowing into the crack tip.

4.1. Off-Fault Damage as a Source of Mechanical Heterogeneity During Earthquake Rupture

[27] The width of strike-slip fault zones is observed to vary along strike. Anderson *et al.* [1983] documented wide variations in the thickness of exhumed parts of the San Gabriel Fault. While the damage zone is only a few cm thick at its narrowest, only one kilometer to the east the damage zone spans tens of meters. Our experiments imply that such changes in the width of the damage zone can have large effects on the rupture velocity during the course of an earthquake, with important consequences for strong ground motion. It is possible that variations in damage zone dimensions may be the physical manifestation of the asperities and barriers on a fault proposed by seismologists to explain high-frequency seismic radiation from earthquakes [Aki, 1979; Papageorgiou, 2003].

4.2. Initial Crack Density and Velocity Reduction

[28] Table 3 shows that $\bar{v}_s / v_s \approx 0.75$ to 0.85 in our all-damaged experiments which, for dry samples corresponds to an O'Connell and Budiansky [1974] crack density parameter $\epsilon \approx 0.15$ to 0.3, comparable to the value we measured using stereology. It is not surprising that the theory and experiments are not in perfect agreement since the theory was developed for a dilute array of nonintersecting fractures.

4.3. Increase in Off-Fault Damage

[29] It is interesting to note that we never observed crack growth during our experiments. We suggest this is because the spatial extent of the off-fault stress field of about 1 cm in Homalite is too small to extend the initial cracks in our experiments, which had an average crack length also on the order of 1 cm. It may be possible to generate an increase in off fault damage by using a geological material like marble. The larger elastic modulus in marble translates to a larger interaction distance of several centimeters, while the weak boundaries of the small grains produce a millimeter-scale network of initial damage.

[30] **Acknowledgments.** Ronald Biegel and Charles Sammis would like to acknowledge the generous support of the National Science Foundation grants EAR-0510142 and EAR-0711171 to the University of

Southern California. They would also like to acknowledge the generous support of the U.S. Geological Survey, grant 07HQGR0035 to the University of Southern California. Ares Rosakis would like to acknowledge the generous support of the National Science Foundation, grant EAR-0538307 to the California Institute of Technology. This research was supported by the Southern California Earthquake Center. SCEC is funded by NSF Cooperative Agreement EAR-0529922 and USGS Cooperative Agreement 07HQAG0008. Our thanks to James Rice, Elizabeth Templeton, and Harsha Bhat for many helpful discussions. This is SCEC contribution 1126.

References

- Aki, K. (1979), Characterization of barriers on an earthquake fault, *J. Geophys. Res.*, *84*, 6140–6148.
- Anderson, J. L., R. H. Osborne, and D. F. Palmer (1983), Cataclastic rocks of the San Gabriel fault—An expression of deformation at deeper crustal levels in the San Andreas fault zone, *Tectonophysics*, *98*, 209–251.
- Andrews, D. J. (2005), Rupture dynamics with energy loss outside the slip zone, *J. Geophys. Res.*, *110*(B1), B01307, doi:10.1029/2004JB003191.
- Ashby, M. F., and C. G. Sammis (1990), The damage mechanics of brittle solids in compression, *Pure Appl. Geophys.*, *133*, 489–521.
- Ben-Zion, Y., and C. G. Sammis (2003), Characterization of fault zones, *Pure Appl. Geophys.*, *160*, 677–715.
- Biegel, R. L., and C. G. Sammis (2004), Relating fault mechanics to fault zone structure, *Adv. Geophys.*, *47*, 65–111.
- Biegel, R. L., C. G. Sammis, and A. J. Rosakis (2007), Interaction of a dynamic rupture on a fault plane with short frictionless fault branches, *Pure Appl. Geophys.*, *164*, 1881–1904, doi:10.1007/s00024-007-0251-2.
- Brune, J. N. (2001), Fault-normal dynamic unloading and loading: An explanation for “non-gouge” rock powder and lack of fault-parallel shear bands along the San Andreas Fault, *Eos Trans. AGU*, *82*(47), Fall Meet. Suppl., Abstract S22B-0655.
- Chester, F. M., J. P. Evans, and R. L. Biegel (1993), Internal structure and weakening mechanisms of the San Andreas fault, *J. Geophys. Res.*, *98*, 771–786.
- Chester, F. M., J. S. Chester, D. L. Kirschner, S. E. Scholz, and J. P. Evans (2004), Structure of large-displacement, strike-slip fault zones in the brittle, continental crust, in *Rheology and Deformation in the Lithosphere at Continental Margins*, edited by G. D. Karner et al., pp. 223–260, Columbia Univ. Press, New York.
- Chester, J. S., F. M. Chester, and A. K. Kronenberg (2005), Fracture surface energy of the Punchbowl Fault, San Andreas system, *Nature*, *437*, 133–136, doi:10.1038/nature03942.
- Dally, J. W., and W. F. Riley (2005), *Experimental Stress Analysis*, 4th ed., College House Enterprises, Knoxville, Tenn.
- Heaton, T. H. (1990), Evidence for and implications of self-healing pulses of slip in earthquake rupture, *Phys. Earth Planet. Inter.*, *64*, 1–20.
- Lu, X., N. Lapusta, and A. J. Rosakis (2006), Constraining friction laws by experimental observations and numerical simulations of various rupture modes, *Eos Trans. AGU*, *87*(52), Fall Meet. Suppl., Abstract, S33C-04.
- Lu, X., N. Lapusta, and A. J. Rosakis (2007), Pulse and crack-like rupture in experiments mimicking crustal earthquakes, *Proc. Natl. Acad. Sci. U. S. A.*, *104*, 18,931–18,936.
- O’Connell, R. J., and B. Budiansky (1974), Seismic velocities in dry and saturated cracked solids, *J. Geophys. Res.*, *79*, 5412–5426.
- Palmer, A. C., and J. R. Rice (1973), The growth of slip surfaces in the progressive failure of over-consolidated clay, *Proc. R. Soc. London, Ser. A*, *332*, 527–548.
- Papageorgiou, A. (2003), The barrier model and strong ground motion, *Pure Appl. Geophys.*, *160*, 603–634.
- Rice, J. R. (2006), Heating and weakening of faults during earthquake slip, *J. Geophys. Res.*, *111*, B05311, doi:10.1029/2005JB004006.
- Rice, J. R., C. G. Sammis, and R. Parsons (2005), Off-fault secondary failure induced by a dynamic slip pulse, *Bull. Seismol. Soc. Am.*, *95*(1), 109–134, doi:10.1785/0120030166.
- Sammis, C. G., G. C. P. King, and R. L. Biegel (1987), The kinematics of gouge deformation, *Pure Appl. Geophys.*, *125*, 777–812.
- Samudrala, O., and A. J. Rosakis (2003), Effect of loading and geometry on the subsonic/interfacial transition of a bimaterial interface crack, *Eng. Fract. Mech.*, *70*, 309–337.
- Templeton, E. L., and J. R. Rice (2006), Extent and distribution of off-fault plasticity during seismic rupture including bimaterial effects, *Eos Trans. AGU*, *87*(52), Fall Meet. Suppl., Abstract S34A-01.
- Underwood, E. E. (1970), *Quantitative Stereology*, Addison-Wesley, Reading, Mass.
- Viesca, R. C., E. L. Templeton, H. S. Bhat, and J. R. Rice (2006), Pore fluid pressurization effects on earthquake rupture propagation with inelastic off-fault response, *Eos Trans. AGU*, *87*(52), Fall Meet. Suppl., Abstract S42A-04.
- Xia, K., A. J. Rosakis, and H. Kanamori (2004), Laboratory earthquakes: The sub-Rayleigh-to-supershear rupture transition, *Science*, *303*, 1859–1861.
- Zheng, G., and J. R. Rice (1998), Conditions under which velocity-weakening friction allows a self-healing versus a cracklike mode of rupture, *Bull. Seismol. Soc. Am.*, *88*(6), 1466–1483.

R. L. Biegel and C. G. Sammis, Department of Earth Sciences, University of Southern California, Zumberge Hall, 3651 Trousdale Parkway, Los Angeles, CA 90089, USA. (biegel@usc.edu; sammis@usc.edu)

A. J. Rosakis, Graduate Aeronautical Laboratories, California Institute of Technology, Pasadena, CA 91125, USA. (rosakis@aero.caltech.edu)